Monatomic glass formation through competing order balance

Yuan-Chao Hu [1,6] ✉, J. T. Zhai[2,6], Le-Hua Liu [2] ✉, W. W. Zhang [2], Hai-Yang Bai [1,3], Wei-Hua Wang [1,3] & Hajime Tanaka [4,5] ✉

The phase transformation of single-element systems is a fundamental natural process with broad implications, yet many aspects remain puzzling despite their simplicity. For instance, transition metals, Tantalum (Ta) and Zirconium (Zr), commonly form body-centred cubic crystals when supercooled. However, according to large-scale computer simulations, their crystallisation rates can differ by over 100 times. We reveal that this difference originates from stronger competing ordering effects in Ta than Zr. The key thermodynamic factor governing these kinetics is interfacial energy reduction through pre-ordering in a supercooled liquid state. In Ta, strong competition between crystallisation and quasi-crystallisation occurs through non-classical pathways facilitated by crystal-like preordering and hierarchical icosahedral ordering. Conversely, Zr lacks this competing effect, leading to ultrafast crystallisation. These distinct features influence their glass-forming ability, potentially explaining the experimental synthesis of glassy Ta over other metals. Our findings provide insights into the formation mechanisms of glasses, crystals, and quasi-crystals of chemical elements.

Every substance is composed of chemical elements. Currently, 118 elements have been discovered and are well-organised in the periodic table. These elements can exist in gas, liquid, or solid phases, and many of them have the ability to be either crystalline or non-crystalline in the solid state. Order-disorder phase transformations in elements have been widely studied across various fields, with glass formation recognised as a fundamental and important process.

A substantial portion of the periodic table is occupied by transition metals, which have played a crucial role in human civilisation since ancient times. The amorphisation of these metals has been an important focus of research over the past two decades[1-7]. Through ultrafast quenching, certain body-centred cubic (BCC) metals, such as Tantalum (Ta), can adopt an amorphous structure at the nanoscale[6]. The critical cooling rate R_c is the minimum rate needed to avoid crystallisation and is a key measure of glass-forming ability (GFA), varying over 15 orders of magnitude in metallic glasses. For Ta, $R_c \sim 10^{14}$ K/s, but FCC and HCP metals require even higher rates, though their exact values remain unknown.

From a materials science perspective, GFA refers to how easily a material can be vitrified, which determines the maximum size of the amorphous sample that can be produced in experiments. The MG field began with the discovery of the first amorphous alloy, the Au-Si binary system, by Duwez et al.[8]. Since then, progress has been largely driven by the discovery of new MGs with larger sizes, ultimately leading to the development of bulk MGs. These advances have predominantly relied on trial-and-error experiments to identify new alloy systems with enhanced GFA (lower R_c). The fundamental physical origin of GFA remains unclear, hindering the experimental fabrication of new bulk MGs.

[1]Songshan Lake Materials Laboratory, Dongguan, Guangdong, China. [2]Guangdong Provincial Key Laboratory for Processing and Forming of Advanced Metallic Materials, National Engineering Research Center of Near-net-shape Forming for Metallic Materials, South China University of Technology, Guangzhou, China. [3]Institute of Physics, Chinese Academy of Sciences, Beijing, China. [4]Research Center for Advanced Science and Technology, The University of Tokyo, Tokyo, Japan. [5]Department of Fundamental Engineering, Institute of Industrial Science, The University of Tokyo, Tokyo, Japan. [6]These authors contributed equally: Yuan-Chao Hu, J. T. Zhai. ✉e-mail: yuanchao.hu@sslab.org.cn; liulh@scut.edu.cn; tanaka@iis.u-tokyo.ac.jp

Bulk MGs are mainly found in multicomponent systems, where numerous control parameters − such as topological and chemical order[9] −complicate the identification of GFA origins. While empirical rules exist, they often lack predictive power. To address this complexity, a more manageable approach is needed, one that simplifies the issue into a solvable form using a bottom-up approach. Based on our previous work[9–11], we have found that local chemical ordering, in combination with local topological ordering, plays a crucial role in determining GFA. Similar effects have been confirmed through extensive simulations of thousands of binary alloys[12,13]. In particular, simulations of a patchy particle model show that introducing non-compatible symmetric structures, like icosahedra, greatly enhances glass formation compared to having only crystalline orderings[14]. However, an excess of icosahedra may lead to quasi-crystallisation[15]. Unfortunately, the glass formation mechanism in multicomponent systems may be more intricate than anticipated, involving multiple factors, such as metastable phase competitions, selective crystallisation, and phase separation[16]. The independent role of local topological ordering, however, was not clearly understood.

Motivated by experimental discoveries of monatomic metal vitrification, we simplify the problem using single-component systems to exclude chemical ordering, aiming to uncover fundamental rules of glass formability. The vitrification of single-component systems is tied to a fundamental question: Can GFA be universally measured for any material on Earth through R_c? That is, is the disordered state a fundamental state for all materials, given sufficiently rapid cooling? This has remarkable implications for our understanding of materials science and phase transitions. Considerable efforts in the literature over the past few decades have attempted to address this. For instance, the monatomic metal germanium was vitrified by Angell et al.[5] under high pressure for a small sample. This aligns with a prediction that competing orderings help vitrification near the triple point for water-type liquids[17]. Subsequently, Zhong et al.[6] demonstrated the vitrification of certain BCC metals at an effective cooling rate of 10^{14} K/s, while FCC and HCP metals did not exhibit similar behaviour. More recently, the vitrification of FCC metals became possible through rapid deposition[18], highlighting the importance of icosahedra-like topological orderings[15]. Despite these advances, the physical mechanisms behind glass formation in monatomic metals remain elusive, primarily due to the difficulty of tracking particle-level information. Unravelling these mechanisms is crucial. Furthermore, understanding the GFA of monatomic metals can provide valuable insights into the fundamental three-dimensional atomic configurations of glasses, as demonstrated in studies on high-entropy alloys with similar metallic radii[19] and on single-component metals[7].

It has long been believed that local structures formed by atoms, constrained by interatomic interactions, play a crucial role in determining liquid properties[20–22]. With isotropic or centrosymmetric interactions, local icosahedral order is prevalent, expected in all close-packed monatomic liquids[1]. The proposal of local icosahedral order to impede liquid crystallisation traces back to the seminal work by Frank in the 1950s[23]. Over the past two decades, substantial efforts have been dedicated to understanding the role of local icosahedral order in glass formation[15,20,21,24–28].

In particular, local icosahedral order has been experimentally detected in pure metals (Ni, Zr, Fe)[29] and alloys[25,30–32], with first-principles molecular dynamics (MD) simulations providing additional support[24]. The key link between experiments and simulations is the ensemble-averaged structure factor. However, bridging the one-dimensional structure factor to three-dimensional atomic packing is a challenging task. For metallic alloys, experiments were often designed for multicomponent systems that tend to crystallise into icosahedral quasi-crystals[25,30], which can effectively increase the likelihood of detecting local icosahedral order. For example, Kelton et al.[25] observed that the ternary Ti-Zr-Ni system preferentially nucleates into a metastable icosahedral quasi-crystal phase, known as the *i* phase, in

the supercooled liquid. Abundant local icosahedral order plays a crucial role in reducing interfacial energy for quasi-crystallisation[10,15,30,32].

Moreover, the discovery of quasi-crystals remarkably enriched crystallography. Despite extensive studies, their structural mechanism remains elusive. One notable contribution by Keys and Glozter[33] suggests that dodecagonal quasi-crystals form through the assimilation of stable icosahedral clusters. Despite this, the crystallisation kinetics of quasi-crystals in supercooled liquids and their competition with regular crystals are still not well understood. Our study aims to provide answers to these fundamental questions.

The current consensus is that the incompatible symmetry of icosahedra with crystalline symmetries hinders crystallisation[15,23,25], and these local structures are pivotal in controlling MG properties[9]. However, the atomic-scale mechanism of how local icosahedral order controls crystallisation kinetics remains unclear, which is crucial for the fundamental understanding of both glass formation and quasi-crystal formation.

Theoretically, classical nucleation theory (CNT) is one of the most widely used frameworks for describing the crystallisation process of various substances[34]. In CNT, crystallisation is driven by structureless random fluctuations, and the process is typically described as a single-step pathway. However, it has been debated that crystallisation could also happen through a non-classical pathway, which deviates from the predictions of CNT. Non-classical pathways often involve crystallisation occurring through pre-order formed in a metastable liquid state, such as those found in hard-sphere[35] and metallic glass-forming liquids[10]. These intermediates offer alternative routes to crystallisation, highlighting the process's complexity. Understanding these mechanisms could provide crucial insights into controlling glass formation.

In this study, we address these fundamental problems of phase orderings through computer simulations, using monatomic metals forming BCC equilibrium crystals, Ta and Zr, as prototypical systems. The absence of chemical complexity ensures a straightforward interpretation of their properties. By directly assessing Time-Temperature-Transformation (TTT) curves and R_c through examining crystallisation kinetics across a wide range of undercooling degrees, we confirm that Ta exhibits a remarkably lower R_c by two orders of magnitude compared to Zr. Minimal differences in crystallisation driving force and diffusion rate between the two systems underscore the decisive role of interfacial energy in crystallisation, aligning with previous findings[9,10,36]. We attribute the observed effect to competing ordering effects. Our analysis reveals a higher abundance of connected icosahedral order in Ta than in Zr, promoting the formation of a quasi-crystalline metastable phase (QCMP) that competes with BCC nucleation. This balanced competition between crystallisation and quasi-crystallisation in Ta occurs through non-classical pathways involving not only local orderings but also their hierarchical orderings. These findings clarify the role of local icosahedral order in glass formation, crystallisation, and quasi-crystallisation of monatomic metals, with potential extrapolation to binary and multi-component systems. The hierarchical nature of particle rearrangements during quasi-crystallisation offers insights into quasi-crystal properties, with potential relevance to other fields.

Results
Computer simulation models
We performed comprehensive MD simulations and data analyses for two transition metals, Ta and Zr, using well-established empirical embedded-atom method (EAM) potentials[6,37]. In the EAM formalism, the total energy of an atom is expressed as

$$E_i = F_\alpha \left(\sum_{j \neq i} \rho_\beta(r_{ij}) \right) + \frac{1}{2} \sum_{j \neq i} \phi_{\alpha\beta}(r_{ij}), \qquad (1)$$

where $\alpha = \beta$ (Ta or Zr) for our single-component systems. Here, F is the embedding energy, which is a function of the local atomic electron

density ρ, itself determined by the pairwise distances r_{ij} between atom i and its neighbours j. The pair interaction ϕ also depends solely on r_{ij}.

We directly extracted these functional terms (F, ρ, ϕ) from the source data of the EAM potentials and plotted them in Supplementary Fig. 1 for both Ta and Zr. In addition, we plotted the corresponding diatomic energy curves as a function of pair distance, calculated for isolated two-atom systems to illustrate the combined effect of the pair and embedding terms. In actual MD simulations, however, the local atomic density is dynamically determined by summing over all neighbouring atoms within a cutoff distance, making the total energy calculation inherently many-body and particularly sensitive to structural disorder.

The EAM potentials employed here were originally constructed by fitting to extensive density functional theory (DFT) calculations, with additional benchmarking against experimental data[6,37]. For example, the melting temperature T_m of the BCC phase − stable in the supercooled liquid region − estimated by MD agrees closely with experimental values for both Ta and Zr[6,10,37–39]. In Ta, the energy differences between various crystal structures relative to BCC are 0.06 eV/atom for β-Ta (σ-phase) and 0.03 eV/atom for A15-Ta (A15 phase), both consistent with experimental measurements and DFT calculations. For Zr, where HCP is the stable phase, the free energy difference between HCP and the metastable BCC phase is 0.0517 eV/atom, again in good agreement with phase stability data from experiments.

To further verify phase stability, we directly calculated the equations of state for several solid phases in both Ta and Zr, as shown in Supplementary Fig. 2. These calculations confirm that BCC is the stable phase for Ta, with A15 and σ as metastable competitors, while for Zr, HCP is the stable phase and BCC and FCC serve as higher-energy competing structures.

Altogether, these EAM potentials reproduce key experimental properties of Ta and Zr, lending confidence to their use in exploring crystallisation kinetics and pathways. Combined with the experimentally consistent differences in GFA observed in both simulation and experiment (see below), these potentials provide a reliable framework for uncovering the underlying physical mechanisms (see more computational details in 'Methods').

Structures and the associated order parameters

Tantalum (Ta) has attracted considerable attention in recent years for its ability to form a glass at ultrahigh cooling rates[6], making it an important model system for studying amorphous structures experimentally[7]. In terms of ordered phases, Ta can crystallise into either the BCC phase (BCC-Ta) or into QCMPs, specifically the σ- and A15-type structures (denoted as σ-QCMP and A15-QCMP, respectively). The σ-QCMP phase is structurally related to β-Ta, and we adopt this terminology for consistency throughout our analysis. In the following, we use the term QCMP to refer collectively to both the σ- and A15-type QCMPs[40,41].

To gain deeper insight into these phases, we first analyse their atomic structures and identify appropriate order parameters for characterising the simulation trajectories at the atomic scale. This structural characterisation helps elucidate how local atomic arrangements contribute to the formation of the different ordered phases. To this end, we employ standard structural data obtained from the Materials Project database[42], which we replicate to construct larger atomic configurations for visualisation and further analysis.

For the regular BCC crystals, we employ the solidity parameter s_6, which is based on the sixth-order ($l = 6$) bond-orientational order parameter[9,43,44]:

$$s_l(i) = \sum_j H \left(\frac{\sum_{m=-l}^{l} q_{lm}(i) q_{lm}^*(j)}{\sqrt{\sum_{m=-l}^{l} |q_{lm}(i)|^2} \sqrt{\sum_{m=-l}^{l} |q_{lm}(j)|^2}} - s_0 \right), \quad (2)$$

where '*' denotes complex conjugation, and $q_{lm}(i)$ is the averaged spherical harmonic component evaluated at the angular positions of particle i relative to its instantaneous neighbours j in the thermal state. The definition of neighbours varies depending on the specific structural motif being characterised (BCC, QCMP, or local icosahedral order), and is described in detail in the 'Methods' section. $H(x) = 1$ if $x > 0$ otherwise $= 0$. To characterise the BCC structure, we define $s_0 = 0.7$. A particle is considered part of the BCC solid if $s_6 > 10$. These thresholds are motivated by previous studies[9,10,43,44].

Nevertheless, quasi-crystalline structures are inherently more complex, exhibiting long-range aperiodicity. Their periodic approximants are complex, yet conventional, crystals whose local structural motifs mimic portions of the true quasi-crystal. In this study, we refer to the σ quasi-crystalline approximant simply as the σ phase, which serves as a periodic analogue of the underlying quasi-crystalline order. Due to the metastable nature of these quasi-crystalline phases and the extensive simulation times required for their full formation, obtaining a complete quasi-crystal was infeasible in our simulations. Instead, we observed only fragments of quasi-crystalline structures. The two approximants identified were the σ phase and the A15 phase, both of which have also been observed in the Dzugutov model, where they contribute to the formation of dodecagonal quasi-crystals[33].

The structure of BCC appears simpler than that of QCMP, as evident from their pair correlation functions $g(r)$ in Fig. 1a. For A15-QCMP, the $g(r)$ also exhibits discrete peaks similar to those in BCC-Ta, albeit with a greater number of peaks. The standard A15 structure adopts a cubic lattice system with 8 atoms per unit cell. However, for σ-QCMP, the structure is more complex than that of A15-QCMP, consisting of 30 atoms per unit cell and adopting a tetragonal lattice system. Additionally, its $g(r)$ appears more intricate with 'noisy' peaks, suggesting complex local environments. Although the overall structure remains ordered, the broad distribution of pair distances reflects the presence of local disorder effects.

To characterise the atomic-scale structure of QCMP, we employ another solidity parameter s_{12} (see Eq. 2)[33], albeit with several key differences from s_6. The solidity parameter (s_{12}) is conceptually equivalent to the solid bond number. We observed that QCMP structures resemble the quasi-crystalline approximants identified by Keys and Glotzer in their single-component model liquid[33]. Consequently, we adopted their method to characterise QCMP. Specifically, since quasi-crystalline phases typically feature larger structural units, we define neighbours as atoms within a distance of 7.7 Å (approximately the 3rd coordination shell) as neighbours. Using Eq. (2), we define the particle-level s_{12} based on the bond properties between a central particle i and each of its neighbours j. A bond is classified as solid-like if $s_{12} > s_0$ and liquid-like if $s_{12} \leq s_0$, otherwise, where we set the threshold $s_0 = 0.45$. The s_{12} value, which counts the number of solid-like bonds, serves as a measure of solidity. Specifically, we classify atoms with $s_{12} > 50$ as solid. This relatively high threshold will be further justified below. Through tests with perfect structures, we found that s_{12} effectively characterises both σ-QCMP and A15-QCMP, and is also capable of identifying BCC, unlike s_6. Therefore, we combine s_{12} and s_6 to achieve a more comprehensive characterisation of QCMP (see 'Methods' for the quantitative criteria).

We first use these order parameters to characterise standard σ-QCMP and A15-QCMP. Then, we analyse them, focusing on local structural orders, particularly local icosahedral order. In Fig. 1b (left panel), an enlarged plane view of the σ-QCMP structure is displayed, with some typical units shown by the solid networks[45]. Atoms are colour-coded based on their local environments, quantified by the number of neighbours within the defined cutoff. Specifically, the solid bond numbers from s_{12} for the blue, cyan, green, red, and yellow particles are 96, 98, 104, 105, and 108, respectively. In this 16170-atom configuration, their concentrations are approximately 6.7%, 26.7%, 26.7%, 26.7%, and 13.3%, respectively.
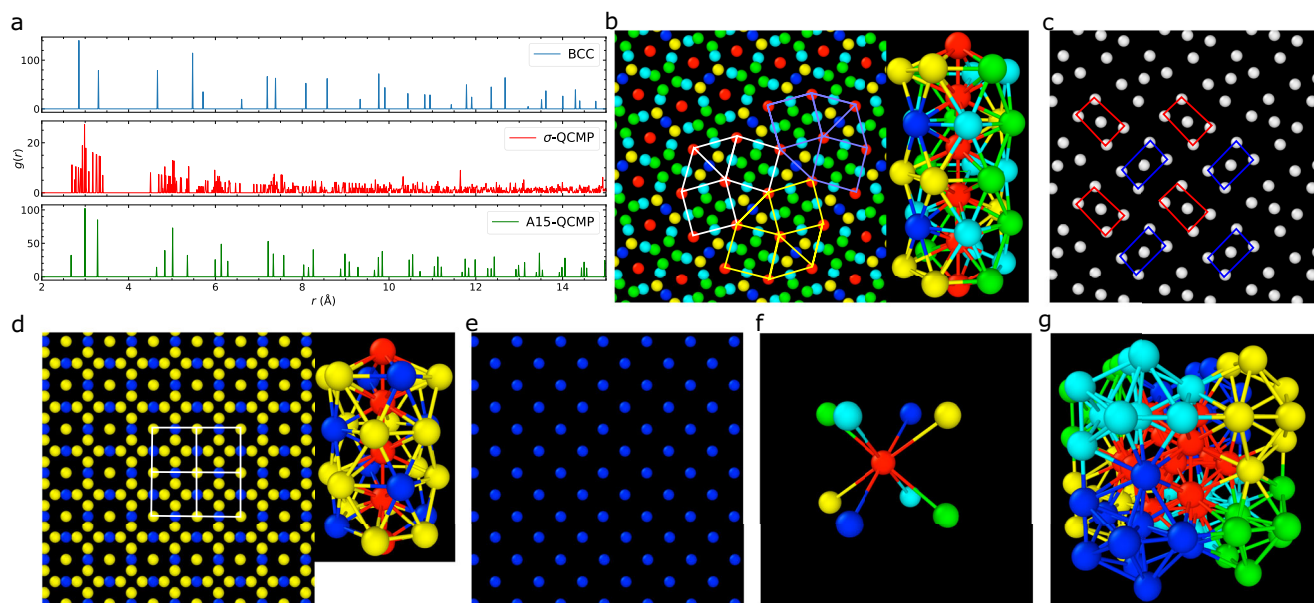
Fig. 1 | Structure analysis of the ordered phases of Ta. a Pair correlation functions of the three phases. **b, c** Features of σ-QCMP, while **d**–**g** highlight characteristics of A15-QCMP. **b** Left panel: A planar view of σ-QCMP, where solid networks indicate typical structure motifs. Right panel: A three-dimensional layered structure of σ-QCMP. Colours in both panels indicate the number of neighbouring particles used in calculating s_{12}. **c** Spatial distribution of icosahedral centres. Solid squares indicate the arrangement of five-membered rectangular units, illustrating their simple layered packings in red and blue. **d** Left panel: A planar view of A15-QCMP with white squares marking typical structure motifs. Right panel: A three-dimensional layered structure of A15-QCMP, centred at the vertices of the white squares.

Colours represent coordination numbers used in calculating s_{12}; yellow atoms at the vertices are replaced by red for clarity. **e** A planar view of the spatial distribution of icosahedral centres forming a BCC lattice. **f** A BCC unit cell formed by icosahedral centres, with atoms and bonds artificially coloured for better visualisation. The icosahedral centres do not directly bond with one another. **g** Full configuration of (**f**) with 12 neighbours added for each icosahedral centre. Neighbours are coloured according to their corresponding centre. The red icosahedron represents the centre of the BCC lattice. These icosahedra share neighbours to form the BCC superlattice structure, with only 81 atoms shown in (**g**).

Of particular interest are the blue and cyan atoms representing icosahedral centres, identified by the bond-orientational order parameter w_6[9]. The definition and calculation of w_6 are provided in the 'Methods' section. Following Russo et al.[44], atoms with $w_6 < -0.023$ are identified as icosahedral centres. Thus, around one-third of the particles in σ-QCMP exhibit icosahedral features. Inspired by the spatial alignment of the red particles, we present one of their three-dimensional packings in Fig. 1b (right panel). Notably, the red particles and the six-member rings intertwine in space, forming two types of six-member rings: one with two icosahedra and the other with three icosahedra. Two red atoms form a Frank-Kasper bond, resulting in two distinct types of such bonds. The Frank-Kasper bond is defined as a pair of neighbouring atoms that share exactly six common neighbours[46]. When considering only the icosahedra, they form rectangles with two different orientations (Fig. 1c), corresponding to the two types of six-member rings. Each layer, or icosahedral unit, i.e. the rectangle (red or blue), exhibits a simple packing feature in space. Therefore, σ-QCMP presents three distinct types of layered structures constructed from icosahedra. The complex hierarchical arrangement accounts for the noisy peaks observed in $g(r)$.

Next, we proceed to examine the structure of A15-QCMP in a similar manner. This phase has been observed in undercooled Ta by droplet experiments[47]. In Fig. 1d (left panel), we present an enlarged plane view of A15-QCMP, with the typical structure indicated by the white squares. In this 16224-atom configuration, the atoms are colour-coded based on their local environment, quantified by their number of neighbours within the cutoff. There are only two types of atoms: the yellow atoms, with 104 neighbours, account for 75% of the total atoms, while the blue atoms, with 110 neighbours, represent icosahedra.

Similarly, in Fig. 1d (right panel), we analyse the three-dimensional packing around the vertices of the unit structure, where yellow atoms located at the white squares are replaced by red for clearer visualisation. The red atoms and the six-member ring iterate in space to construct the three-dimensional structure, with each ring containing two icosahedra facing each other. Although the ring rotates to the adjacent one, only one type of Frank-Kasper bond is formed by two red particles in the A15 phase. Interestingly, when considering only the structure of the icosahedra (Fig. 1e), they arrange themselves in the BCC lattice, as shown in a local example in Fig. 1f. Note that these icosahedra are not directly bonded but connected through the vertices of the icosahedral clusters. Reintroducing the neighbouring atoms of these icosahedra reveals a 'big BCC' structure in Fig. 1g, where each lattice point is occupied by an icosahedral cluster. Therefore, A15-QCMP shares some packing features with the BCC of Ta, as observed in their $g(r)$. The less complex local structure in A15-QCMP also explains its $g(r)$ difference from σ-QCMP in Fig. 1a[48].

The existence of different types of Frank-Kasper bonds in monatomic supercooled liquids may help elucidate why such local structures can stabilise the supercooled liquid state[46]. In addition, both types of structural orderings impose constraints on the study of supercooled liquids by first-principles calculations, given the relatively small size of simulation systems.

Crystallisation kinetics

Using the relevant structural order parameters identified above, we analyse the crystallisation kinetics of Ta and Zr at various undercooling levels T/T_m, where T_m denotes the melting point of their respective BCC phase[10]. This convention is used throughout the paper unless stated otherwise. We conducted comprehensive isothermal annealing simulations near the nose temperature, which corresponds to the temperature on the TTT curve where the shortest time is required for a specific phase transformation. These simulations confirm that Ta can
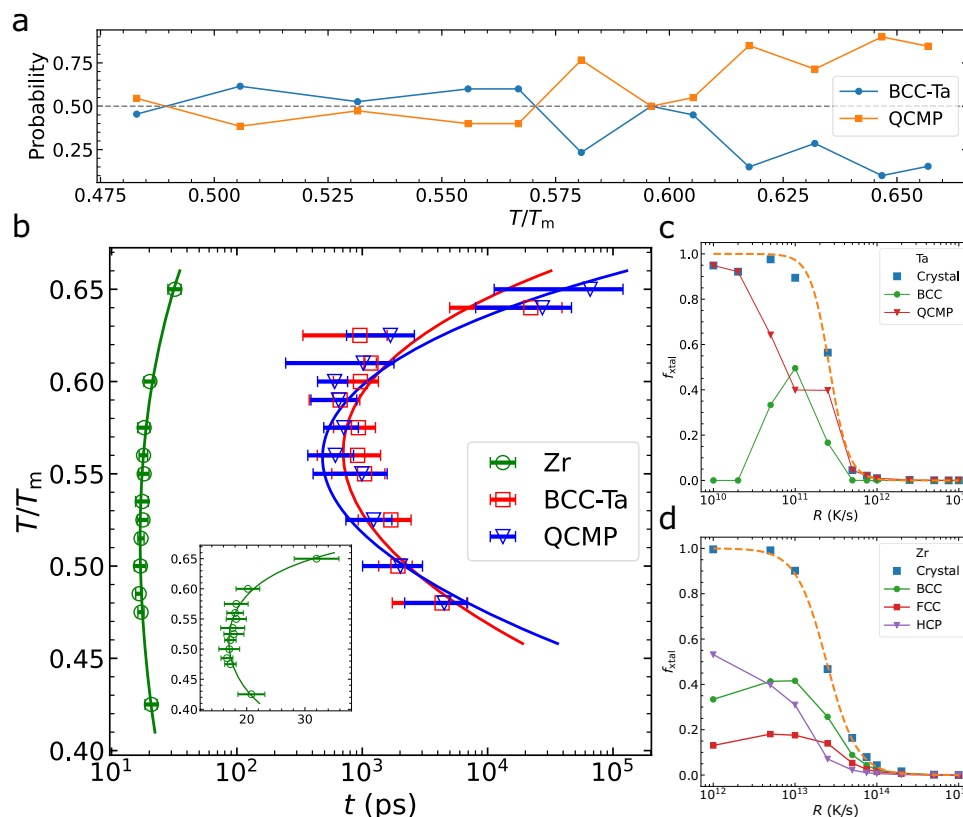
Fig. 2 | Characterisation of crystallisation kinetics. a Probability of obtaining either BCC or QCMP as the final phase, based on 30 independent simulations conducted at each temperature for undercooled Ta. **b** TTT curves of Zr and Ta, showing the crystallisation times τ_{xtal} as a function of temperature in the super-cooled liquid region. Error bars represent statistical variations from independent simulations. For Ta, TTT curves were measured for BCC and QCMP separately. The inset displays an enlarged TTT curve for Zr. For (**a**, **b**), QCMP primarily appears as the σ phase, while A15 is rarely observed; therefore, only σ-QCMP is considered here. The solid lines represent fits to Eq. (3). **c** Fraction of crystallised atoms f_{xtal} at varying cooling rates R for Ta. An orange dashed line represents a sigmoid-like fit. Crystallised atoms are further categorised into BCC and QCMP structures. The fraction of BCC atoms peaks around R_c, but QCMP structures predominate, particularly at low R. **d** Analysis for Zr follows the same procedure as for Ta. During crystallisation, the BCC phase competes with a mixture of FCC and HCP structures, with HCP dominating at low R.

crystallise into either BCC or QCMP, whereas Zr only forms crystalline phases (BCC or HCP). For Zr, the stable phase at ambient temperature and pressure is HCP, while BCC becomes the equilibrium crystal structure at elevated temperatures. Therefore, we refer to Zr in terms of its BCC phase throughout this study.

In Fig. 2, we present two sets of simulations. The first set consists of thermal annealing at constant temperatures (panels a and b), with 30 independent simulations performed at each temperature. In these simulations, we track the trajectories and analyse the fractions of different structures. The final products are typically either BCC or σ-QCMP, with A15-QCMP appearing only rarely. The fraction of trajectories that result in BCC and QCMP was calculated and is presented as probabilities in Fig. 2a. Above $0.6T_m$, QCMP formation is much more likely than BCC. whereas at lower temperatures, the probabilities become comparable. This observation, together with the atomic-scale processes discussed below, suggests that σ-QCMP nucleates most easily from the supercooled liquid, while A15-QCMP is the most difficult to nucleate.

Using the same grouping method, we define the nucleation time for each simulation as the time at which the fraction of atoms in the ordered phase reaches approximately 5%. We tested different threshold values and confirmed that the results remain qualitatively consistent. In addition, we performed simulations with $N = 16,000$ particles at relatively low temperatures ($0.475 \leq T/T_m \leq 0.650$), where a 5% threshold is sufficient for characterisation. Specifically, for Ta, we measure the incubation times for the nucleation of BCC and QCMP

separately. We then construct the TTT curves for BCC and QCMP in Ta, and compare them to those of Zr, as shown in Fig. 2b. These curves are well described by the CNT (see below). Zr exhibits rapid crystallisation, with a nucleation time as short as 16 ps. In contrast, both BCC-Ta and QCMP require approximately 1000 ps for nucleation[49]. Interestingly, the TTT curves for Ta's BCC and QCMP phases nearly coincide, indicating a balanced competition between the orderings within this temperature range. This balance leads to intriguing phase transformation characteristics. Therefore, understanding the crystallisation kinetics of both phases and their competition is essential for understanding GFA.

Competing orderings are also observed in other systems. For instance, in a sphere-forming block copolymer[50], both the BCC phase and the Frank-Kasper σ-phase can form. However, they exhibit stability in distinct temperature ranges, resulting in two distinct noses in the TTT diagram. This imbalance in competing orderings arises from the preference for different phases at varying temperatures. Thus, we anticipate more intriguing competition-induced crystallisation pathways in undercooled Ta compared to the block copolymer.

The second set of simulations involves quenching at different cooling rates. We analyse the structures of the low-temperature solids, with the results presented in Fig. 2c, d for Ta and Zr, respectively. Due to the ultrafast cooling process, multiple phases can nucleate and grow, resulting in a mixture of structures in the final products. These simulations provide a direct measurement of R_c. We quantified the cooling rate (R) dependence of the fraction of crystallised atoms (f_{xtal}).
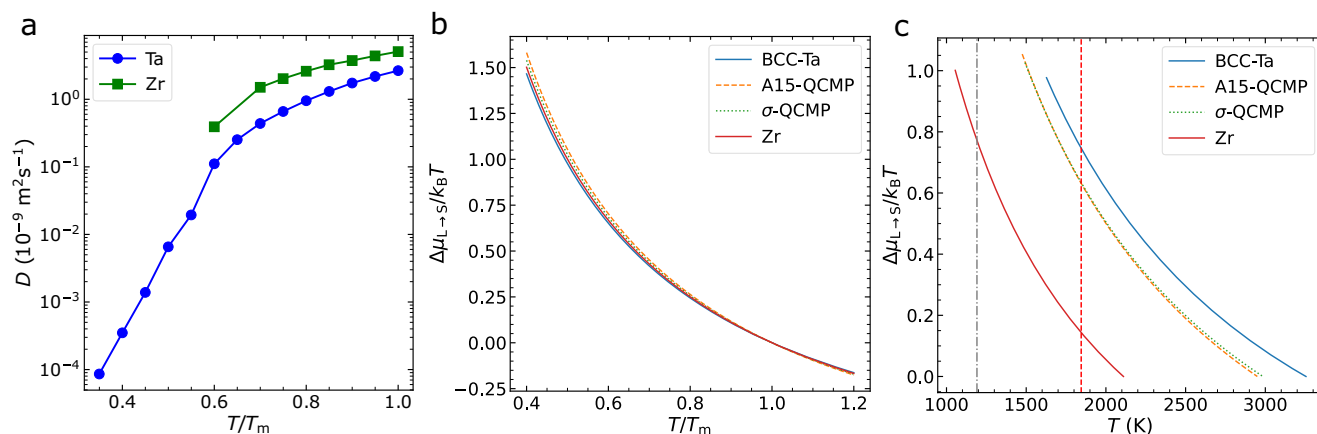
Fig. 3 | Analysis of crystallisation factors. a Diffusion coefficients in supercooled liquids for Ta and Zr. Zr readily crystallises at large supercoolings, limiting the temperature range for measuring its diffusion rate. Ta exhibits slower diffusion compared to Zr, but their diffusion coefficient ratio is approximately D(Zr)/D(Ta) ≈ 2.14 at the same T/T_m. T_m refers to the melting temperature of the BCC phase for each metal. **b** Increase in the reduced thermodynamic driving force of nucleation, $\Delta\mu_{L\to S}/k_B T$, as T/T_m decreases. T_m refers to the melting temperature of each corresponding phase. At a certain T/T_m, the $\Delta\mu_{L\to S}/k_B T$ values for all phases are nearly identical. **c** T-dependence of $\Delta\mu_{L\to S}/k_B T$ for different phases. The red-dashed and grey-dot-dashed lines represent about $0.57T_m$ for Ta and Zr, respectively.

In Fig. 2c, the critical cooling rate of Ta is estimated at $R_c \approx 2.62 \times 10^{11}$ K/s, with a fifty percent chance for liquid crystallisation[14]. Notably, QCMP is the predominant product, consistent with results from isothermal annealing simulations at higher temperatures (Fig. 2a). In contrast, the estimated R_c for Zr is ~2.43×10^{13} K/s (Fig. 2d)[9], approximately 1% of Ta's value. This supports the conclusions drawn from the TTT curves. The crystalline product in Zr is mostly BCC or HCP, lacking QCMP, indicating weaker frustration compared to Ta. This finding aligns with our previous observations using a patchy particle model, where mixtures containing crystal-like symmetry motifs with icosahedral symmetry motifs exhibited better GFA than those with only crystal-like symmetry motifs[14].

Classical nucleation theory analysis

From CNT[34], the kinetics of crystallisation is determined by both the nucleation rate and the crystal growth speed. Although the crystal growth rate of Zr is faster than that of Ta, it is only three times faster[10], far below the two orders of magnitude difference. Therefore, the crucial factor determining the overall crystallisation kinetics is the nucleation rate I, defined as the number of nucleation events per unit time in a given volume V. It is related to the nucleation time τ_{xtal} through $\tau_{xtal} = (I \cdot V)^{-1}$ [51]. Hence, we can express τ_{xtal} as:

$$\tau_{xtal} = \tau_0 D \exp\left(\frac{\alpha\gamma^3}{\Delta\mu_{L\to S}^2 k_B T}\right), \qquad (3)$$

where τ_0 is a prefactor, D is the translational diffusion coefficient, $k_B T$ is the thermal energy, and α is a factor accounting for the shape of the crystal nucleus. γ is the thermodynamic interfacial tension, and $\Delta\mu_{L\to S}$ is the thermodynamic driving force from the liquid phase to the solid phase. Therefore, the key factors controlling τ_{xtal} (i.e. I) are D, $\Delta\mu_{L\to S}$, and γ.

Now, we discuss their effects in Ta versus Zr. Firstly, we calculated the diffusion coefficient in the supercooled states (see 'Methods'). Zr is prone to crystallisation at strong undercooling conditions, limiting our access to a narrow temperature range. On the other hand, the formation of local icosahedral order and Frank-Kasper bonds in Ta can effectively stabilise the supercooled liquid[46]. However, Fig. 3a shows that at the same undercooling degree, their diffusion rate difference is only about a factor of two.

We also estimated the thermodynamic driving force, $\Delta\mu_{L\to S}$, for the different ordered phases of Ta and compared them to Zr using an empirical approach based on the measured enthalpy of fusion, ΔH_m. For Ta, BCC and QCMP do not necessarily share the same melting temperature, T_m, due to their distinct structures. Therefore, we determined their respective T_m values using the two-phase coexistence method (see 'Methods') and found that QCMP has a lower T_m than BCC. We then calculated ΔH_m for each phase at its corresponding T_m (see 'Methods' and Supplementary Fig. 3). The estimated values of ΔH_m are 0.274 ± 0.027 eV/atom for BCC, 0.264 ± 0.027 eV/atom for σ-QCMP, and 0.268 ± 0.028 eV/atom for A15-QCMP, indicating that the stable BCC phase has the highest ΔH_m. Using the same procedure, we characterised Zr and found its ΔH_m to be 0.180 ± 0.015 eV/atom (see Supplementary Fig. 4). Furthermore, as shown in Fig. 3b, the differences in the $k_B T$-reduced $\Delta\mu_{L\to S}$ among these phases are minimal at a given T/T_m. It is also worth noting that the differences remain very small at a given temperature (see Fig. 3c). The slight variations at reduced temperatures may arise from small differences in T_m, while uncertainties associated with the empirical estimation of $\Delta\mu_{L\to S}$ from ΔH_m could also contribute to minor discrepancies. However, since these differences are relatively small, they do not greatly affect the subsequent analyses. In addition, the slightly lower driving force of the σ-phase, combined with its more frequent nucleation observed in Fig. 2a, further implies its lower interfacial energy.

While the diffusion rates and thermodynamic driving forces for these phases are similar, their crystallisation behaviours and structural properties can vary remarkably. As shown in Fig. 2a for Ta, at weak undercooling, the final ordered product is predominantly σ-QCMP, while A15-QCMP is much rarer compared to the BCC phase. Analysis of the radial distribution function, $g(r)$, in Fig. 1a reveals that σ-QCMP exhibits a highly complex local structure, resembling the liquid state more closely than the other phases. In contrast, A15-QCMP displays a well-ordered structure similar to BCC but with a more hierarchical arrangement, making it more distinct from the liquid. This structural complexity suggests that QCMP nucleation, particularly for the A15 phase, involves higher free energy barriers. The extensive atomic rearrangement required to establish the ordered structure leads to significant entropy loss, further hindering nucleation. As shown in Fig. 2a, the σ phase nucleates more readily at lower undercoolings and becomes increasingly comparable to the BCC phase at deeper undercoolings. Its slightly faster nucleation kinetics is also evident from the TTT curves in Fig. 2b. Given the similar thermodynamic driving forces and diffusion constants among these phases, we anticipate that A15-QCMP possesses the highest liquid-solid interfacial energy, while σ-
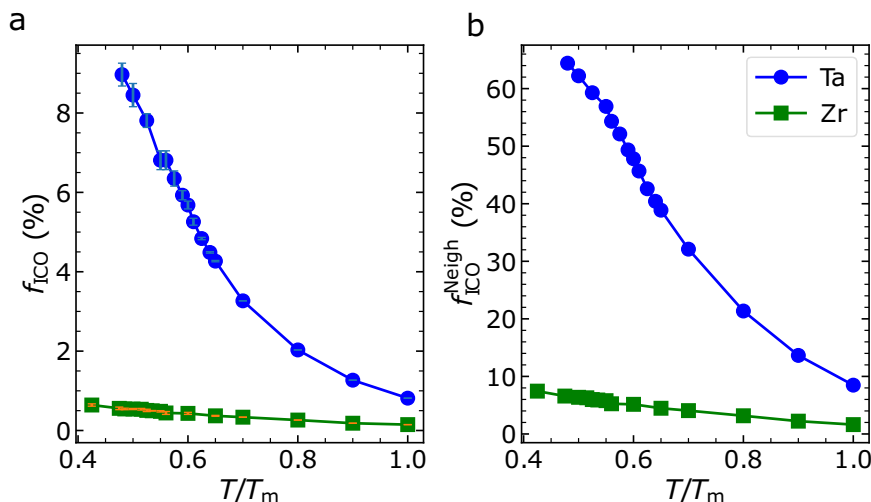
Fig. 4 | Local icosahedral order and its spatial connections in undercooled liquids. a The fraction of local icosahedral ordering, f_{ICO}, in Ta compared to Zr. The number of local icosahedral orders increases drastically in Ta with increasing degree of undercooling, while that of Zr only mildly grows. **b** The fraction of atoms involved in icosahedra, f_{ICO}^{Neigh}. We count all the atoms identified as the centres of icosahedra along with their 12 neighbours, ensuring no double counting. This approach captures both isolated icosahedra and connected icosahedra, which represent short-range and medium-range ordering, respectively.

QCMP exhibits the lowest. Additionally, the faster crystallisation rates observed for Zr compared to Ta in Fig. 2b suggest that Zr has the lowest liquid-crystal interfacial energy among these phases.

To validate our conjecture, we directly analysed the liquid-crystal interfacial energy from our simulations. Building on the work of Tanaka and co-workers[36], the interfacial energy is proportional to the square of the structural order parameter gradient at the interface, as described by the general Ginzburg-Landau theory ($\gamma \propto \left(\frac{\partial Q}{\partial x}\right)^2$, where Q represents the structural order parameter and x is the coordinate perpendicular to the interface). This gradient decreases as the interfacial thickness increases and the structural contrast decreases. Consequently, a thicker interface with reduced structural mismatch leads to a smaller gradient, thereby lowering the interfacial energy. To estimate the interfacial energy, we characterised the atoms at different liquid-solid interfaces in equilibrium (see 'Methods'). Briefly, we first calculated the free energy difference arising from the presence of liquid-solid interfaces at T_m using the free energy perturbation method. We then equilibrated a liquid-solid coexistence configuration with two planar interfaces at T_m and analysed their properties, including the number of atoms belonging to the interface and the interfacial area obtained from morphology analysis. From this approach, we estimated the interfacial energy $\gamma(T_m)$ as 1.182, 1.162, and 1.495 eV/nm² for BCC, σ-QCMP, and A15-QCMP of Ta, respectively. For Zr, the BCC phase exhibits a significantly lower interfacial energy of 0.542 eV/nm². These results are consistent with our analysis of crystallisation kinetics, CNT, and structural features. Additionally, an intriguing observation emerges from the interface morphology (Supplementary Fig. 5): the surface mesh of the BCC phase appears rugged, particularly for Zr, whereas the QCMP phase exhibits relatively smoother, flatter interfaces. This difference likely reflects their respective interfacial energies. The observed interface morphology warrants further investigation in future studies.

Using the diffusion rates, thermodynamic driving forces, and liquid-solid interfacial energies for different phases, we fitted the TTT curves to Eq. (3). As shown in Fig. 2b, Eq. (3) provides an excellent fit to the data. In the fitting process, we independently determined D, $\Delta\mu_{L\to S}$, and γ, while leaving the remaining parameters as free fitting variables.

These results underscore the critical role of interfacial energy in governing overall crystallisation kinetics, consistent with our previous study comparing Zr to binary alloys NiAl, CuZr, and CuZr$_2$[9]. However, the underlying mechanism differs. In these binary systems, we identified local chemical order, in addition to local topological order, as the key factor influencing interfacial energy. In contrast, the absence of chemical ordering effects in the current case suggests that the governing mechanism arises from competing orderings[20,36].

Considering interfacial energy, we thoroughly analysed local icosahedral order in the equilibrium liquid. It is revealed that local icosahedral order introduces frustration against crystallisation and is an essential component in the formation of QCMP. First, we examined the temperature dependence of the fraction of the local icosahedral order (see Fig. 4a). In Zr, this fraction remains low, increasing slowly with decreasing temperature[24]. Conversely, Ta shows a notably higher fraction of local icosahedral order, which rapidly increases during undercooling. Additionally, an important distinction emerges when examining neighbouring particles of icosahedra, particularly the clusters of local icosahedral order, which serve as bridges for constructing medium-range orders. Comparison between Fig. 4a and b reveals a significant spatial connection of local icosahedral order in Ta. For 8% of atoms identified as local icosahedral order (f_{ICO} around $T/T_m \sim 0.5$ in Fig. 4a), the total number of atoms involved in local icosahedral clusters would reach 104% if there were no connections between them. However, this fraction is approximately 60% (see Fig. 4b), indicating robust spatial connectivity that is crucial for QCMP formation.

These results suggest that medium-range orderings formed by local icosahedral order impede crystallisation by increasing the interfacial energy of BCC nucleation. Notably, since the crystallisation kinetics are similar between BCC and QCMP of Ta (see Fig. 2b), local icosahedral order may instead reduce the interfacial energy of QCMP nucleation (further discussed below). However, we emphasise that local icosahedral order, although some may be directly centre connected[52,53], does not inherently possess extensive spatial extendability[54]. Thus, the effects may be weak. Furthermore, despite stronger medium-range orderings in Ta compared to Zr, their diffusion rates show no remarkable differences (Fig. 3a). Thus, local icosahedral order primarily influences crystallisation rather than decelerating dynamics[55].

Atomic-scale crystallisation mechanism

Recognising the critical role of local icosahedral order in Ta crystallisation, our goal is to elucidate the underlying atomic-level physical
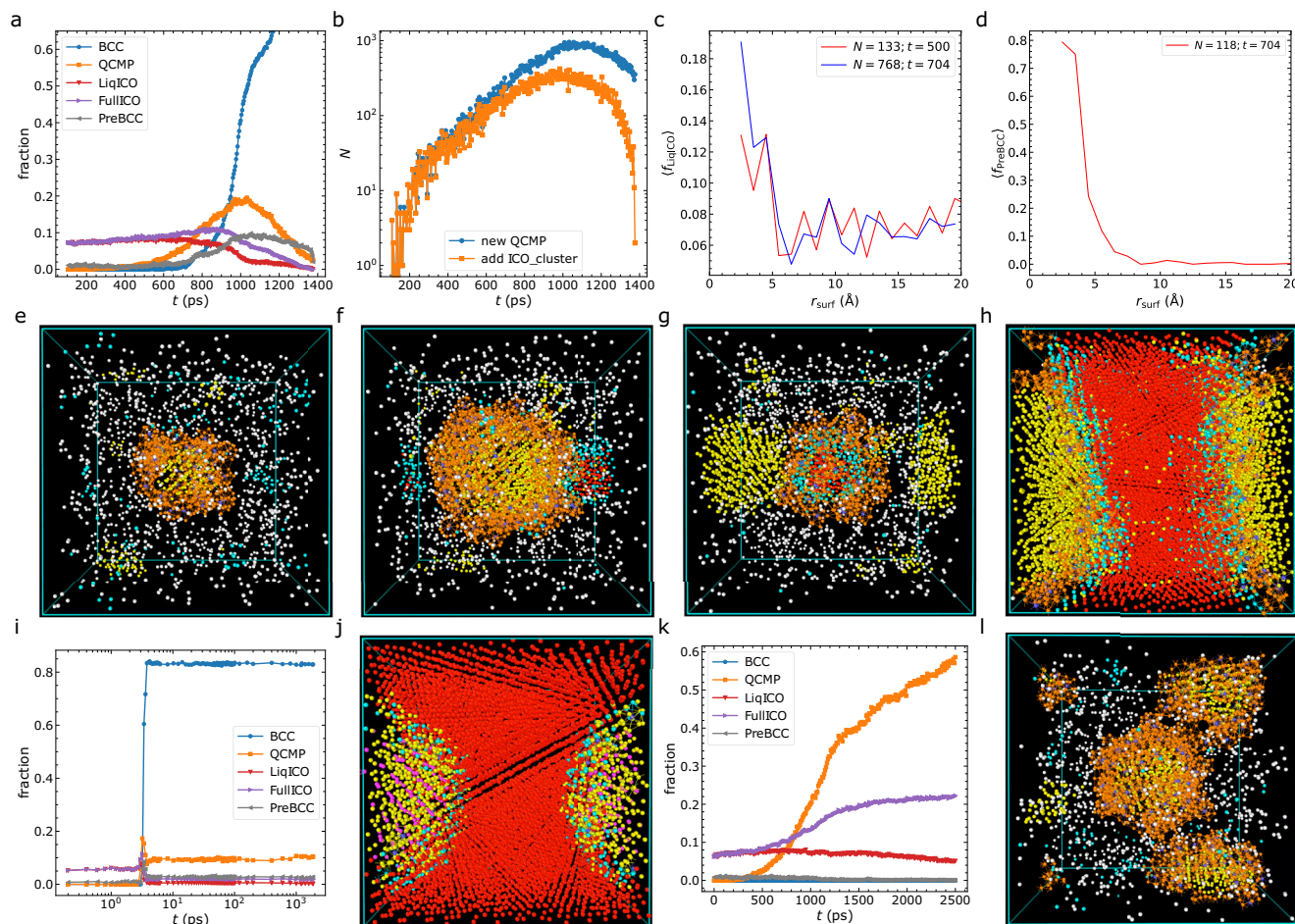
Fig. 5 | Crystallisation pathways of undercooled Ta. The exemplified temperature is approximately $0.57T_m$. **a**–**h** BCC crystallisation accompanied by σ-QCMP pre-nucleation and growth. **a** Time dependence of different types of structural orderings towards BCC crystallisation (LiqICO: local icosahedral order in the liquid phase; FullICO: all local icosahedral order in the system; PreBCC: BCC preordering). Preorderings exist for both BCC and QCMP. **b** Cluster attachment of local icosahedral clusters to newly formed QCMP. The blue symbol represents the newly formed QCMP phase at each t_0, compared to its previous adjacent configuration at t_0-4 ps, while the local icosahedral clusters incorporated into QCMP are shown in orange. **c** Density profile of local icosahedral order from the surface of QCMP. N represents the number of atoms within QCMP, and t denotes time. **d** Density profile of BCC preorderings from the surface of BCC. N represents the number of atoms in

BCC. Visualisation of QCMP growth from $t = 500$ ps (**e**) to $t = 704$ ps (**f**). The QCMP nucleus is re-centred for better visualisation. Visualisation of BCC growth from $t = 704$ ps (**g**) to $t = 1024$ ps (**h**). The BCC nucleus is re-centred for better visualisation. **i** Rapid crystallisation towards BCC coexisting with A15-QCMP. The occurrence of A15-QCMP is much rarer than that of σ-QCMP. **j** Snapshot of the final product of case (**i**). **k** Crystallisation towards σ-QCMP with the absence of BCC. **l** Visualisation of σ-QCMP crystallisation at $t = 620$ ps of case (**k**). In all snapshots, white atoms represent LiqICOs, yellow denotes σ-QCMP, and red indicates BCC. Cyan represents PreBCC. Purple represents local icosahedral order at the surface of QCMP, while orange denotes their 12 nearest neighbours. Magenta inside QCMP represents local icosahedral order of the A15 phase.

mechanism. We categorise Ta crystallisation pathways at various supercooling degrees and analyse their atomic-scale features. From our analysis, we found that the crystallisation phases show an interesting dependence on the degree of undercooling (see Fig. 2). However, the atomic-scale crystallisation mechanism, or the crystallisation pathway towards QCMP (or BCC), does not depend on temperature.

From Fig. 2a, we observe that at temperatures above $0.6T_m$, BCC nucleation is suppressed. Instead, QCMP typically nucleates, aided by the lower interfacial energy associated with the medium-range order of local icosahedral order in the supercooled liquid state. However, the low abundance of local icosahedral order at high temperatures can prolong the QCMP nucleation time, contributing to the shape of the TTT curve.

At lower temperatures, both BCC and QCMP have nearly equal nucleation chances, leading to competing ordering pathways. Interestingly, when QCMP is the final product, BCC nucleation does not occur. However, if BCC is the final product, it is often accompanied by QCMP pre-nucleation, with subsequent BCC growth at the expense of

QCMP. In the following, we explore three typical crystallisation situations of Ta through independent isothermal simulations at $-0.57T_m$.

Figure 5a illustrates a typical case of BCC crystallisation mediated by the pre-nucleation and growth of σ-QCMP. Once nucleated, the BCC phase rapidly expands by consuming σ-QCMP. This process is facilitated by the low interfacial energy of σ-QCMP, which allows it to easily transform into either the liquid or BCC phase. Intuitively, one might expect two types of solid-liquid interfaces: liquid-σ-QCMP and BCC-σ-QCMP. However, our simulations reveal that the transformation from σ-QCMP to BCC does not occur directly. Instead, σ-QCMP first transitions into the liquid state at the surface before being incorporated into the BCC phase. This two-step process likely arises from the relatively lower solid-liquid interfacial energy compared to the solid-solid interfacial energy, resulting in a lower barrier for the former. Interestingly, a similar phenomenon was reported by Peng et al.[56] during solid-solid phase transitions in colloidal systems. These findings suggest that crystal growth kinetics under two-phase coexistence conditions may represent a promising direction for future research.

We now shift our focus to the structural orderings involved in the crystallisation process (see 'Methods' for definitions). In the equilibrium liquid, fluctuating local icosahedral order and BCC crystal-like preordering (PreBCC) are present and coexist. PreBCC refers to preordering characterised by BCC-like bond-orientational order and serves as a precursor to the formation of the BCC crystal structure. Previously, we identified the critical role of PreBCC in the nucleation of BCC/B2 phase by wetting the nuclei[9,10], leading to the non-classical crystallisation pathway of metallic liquids. Similarly, since icosahedra are essential components of QCMP (see Fig. 1), we anticipate they serve as preorderings for QCMP nucleation. As σ-QCMP grows, the total number of local icosahedral orders in the system increases while that in the liquid phase gradually decreases.

Monitoring the newly formed σ-QCMP at each time step reveals that a great portion originates from existing local icosahedral order in the liquid phase (LiqICO) from the previous time step. These local icosahedral orders are typically short-lived (Supplementary Fig. 6a) and display specific spatial point patterns[57] rather than random distribution (Supplementary Fig. 6b).

In Fig. 5b, we track the evolution of different phases by analysing a trajectory with snapshots recorded at 4 ps intervals. Specifically, at each time t_0, we compare the structure to its immediately preceding configuration at t_0−4 ps. The blue curve represents the number of atoms newly incorporated into the QCMP phase during this interval, while the orange curve quantifies how many of these newly added QCMP atoms were part of local icosahedral clusters in the previous snapshot. This comparison allows us to determine the origin of the ordered atoms. The overlap between the blue and orange curves before approximately 500 ps in Fig. 5b indicates that the QCMP phase primarily grows by incorporating surrounding local icosahedral clusters during this period. This strongly supports a cluster attachment mechanism as the driving force behind QCMP crystallisation. Further confirmation comes from comparing the total amount of local icosahedral order (Supplementary Fig. 6c) with the number of local icosahedral clusters, which include both the local icosahedral order and their nearest neighbours (Fig. 5b). This is further supported by measuring the density profile of LiqICOs surrounding the surface of the QCMP phase at two different time steps (see Fig. 5c). An enhanced icosahedral density is consistently observed within 1–2 layers surrounding the QCMP nucleus surface, indicating the attachment/addition of the local icosahedral clusters to the QCMP phase. This observation poses a challenge to CNT, which assumes atoms as the unit of ordering. It offers valuable insights into the general growth mechanism of quasi-crystals[33].

The density profile analysis is sensitive to the shape anisotropy of the nucleus, despite its apparent spherical nature (see Fig. 5e, f). To reinforce our findings, we conducted a similar analysis using the bond-orientational order parameter w_6, which is less affected by shape anisotropy (see Supplementary Fig. 6d). These analyses suggest that the growth of σ-QCMP involves the incorporation of icosahedra at its surface. Furthermore, visualising the σ-QCMP nucleus at the same time steps (Fig. 5e, f) reveals its wetting by LiqICOs, effectively lowering interfacial energy and facilitating quasi-crystallisation in undercooled liquids. More specifically, in these panels, we illustrate LiqICOs in two distinct forms based on their proximity to the growing σ-phase nucleus (represented by yellow atoms). The first type is distributed throughout the entire simulation space without considering neighbouring configurations. The second type is located on the nucleus surface, with their centres coloured purple and their neighbours coloured orange. Our analysis reveals that the nucleus is consistently surrounded by this second type of LiqICOs and grows by 'consuming' them (see Fig. 5b). This observation suggests that the nucleus is effectively wetted by LiqICOs, which plays a key role in lowering the interfacial energy and facilitating quasi-crystallisation. This behaviour resembles that of equilibrium crystal formation (see ref. 10,35,36,58 and below). These

results illustrate the hierarchical nature of the non-classical crystallisation pathway of σ-QCMP, progressing from particles to local icosahedral clusters to QCMP. Simultaneously, the enrichment of local icosahedral order on the surface of σ-QCMP suggests that the QCMP nucleus catalyses the formation of local icosahedral order, which explains the sustained presence of local icosahedral order prior to rapid BCC growth (see panel a).

Similar analyses were conducted for BCC. In Fig. 5d, we present the density profile of PreBCC surrounding the BCC nucleus at the time step corresponding to Fig. 5g. The density profile of w_6 shows behaviour opposite to that of LiqICO (Supplementary Fig. 6e). Notably, 1–2 layers of PreBCC consistently surround the BCC nucleus, potentially accompanied by local icosahedral order in the outer layer. This hierarchical structural feature is not unique to Ta but also holds for binary alloys[53]. After nucleation, BCC quickly grows at the expense of the σ-QCMP phase (for example, see Fig. 5h), ultimately causing the latter to disappear. This transformation is facilitated by wetting effects for both phases, and an intermediate disordered phase may arise, warranting further investigation[50]. In this specific case, only one QCMP nucleus is formed. Similar mechanisms are also observed when multiple QCMP nuclei are present (see Supplementary Fig. 7).

In the supercooled liquid, the BCC nucleus is surrounded by PreBCC structures, while the QCMP nucleus (primarily observed for the σ phase) is enveloped by local icosahedral clusters. For BCC, the unit cell of the crystal structure is relatively simple, allowing for easy extension by adding individual particles. In contrast, for the QCMP phase, as discussed above, nucleation and growth proceed by incorporating local icosahedral clusters, rather than simply adding individual particles. Therefore, we emphasise that the non-classical crystallisation pathway of BCC fundamentally differs from that of QCMP, as the former proceeds solely at the particle level.

Figure 5i shows a different case where BCC crystallisation is accompanied by A15-QCMP. Such occurrences are much rarer than those of σ-QCMP. Similarly, BCC is wetted by PreBCC, while A15-QCMP is wetted by LiqICOs. They nucleate roughly simultaneously, albeit with the latter slightly preceding. However, when the two phases meet, neither of them can grow. Our simulations reveal that a thin liquid layer forms at the interface between the BCC and A15 phases. This liquid layer is considerably thinner compared to that in Fig. 5h, with only minimal preordering associated with either the BCC or A15 phases (see Fig. 5j), resulting in a pronounced structural gradient. As a result, the BCC-A15 interface remains relatively stable, and in our long-term simulations (up to 2.0 μs), no crystal growth occurs from either phase. This observation is further supported by the similarity in the ordered structure between BCC and A15-QCMP (see $g(r)$ in Fig. 1a). Both phases exhibit high stability and a high degree of order, further confirming the higher interfacial energy of A15-QCMP than σ-QCMP. We hypothesise that any transformation between these phases would require mediation by an intermediate liquid phase to reduce the energy barrier, similar to the BCC−σ phase transformation observed earlier. In this context, the 'interfacial energies' specifically refer to the liquid−A15-QCMP and liquid−σ-QCMP interfacial energies. This hypothesis explains why σ-QCMP nucleates more frequently, despite A15-QCMP having a larger thermodynamic driving force. Additionally, the results suggest that the interface is more stable for the narrower preordering layer. The discovery of the stable BCC-A15 interface is consistent with previous studies on other transition metals and provides further insight into why enhanced sampling is generally required to accelerate interface migration[59,60].

Due to the metastable nature of the QCMP phases compared to BCC, any QCMP phase should eventually transform into BCC given enough simulation time. However, the exact timescale for this transformation depends on the solid-solid phase transformation kinetics. In our simulations, this transformation occurs more easily for σ-QCMP (see Fig. 5a). Nevertheless, the kinetics can be too slow for this
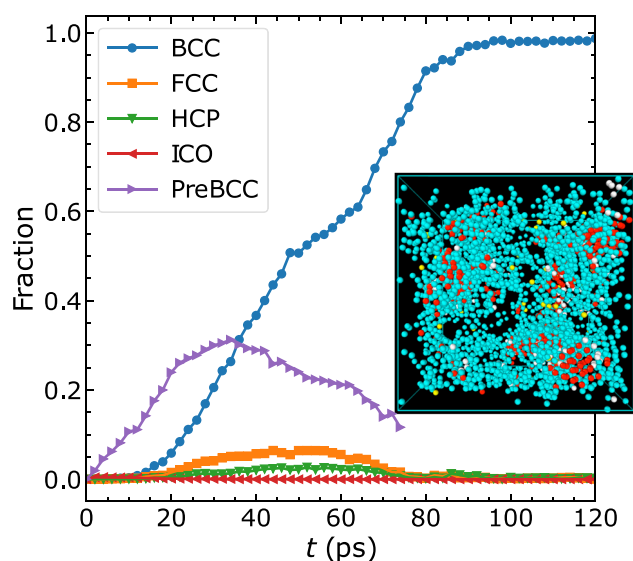
Fig. 6 | Crystallisation mechanism of undercooled Zr. The exemplified temperature is approximately $0.57T_m$. The final crystal product is BCC, which is weakly frustrated by FCC and HCP orderings. The amount of local icosahedral order (ICO) is negligible, but BCC preordering (PreBCC) is considerable. The inset visualises the crystallisation state at $t = 16$ ps. Red atoms represent BCC, white atoms represent either FCC or HCP, yellow atoms represent ICO, and cyan atoms represent PreBCC.

transformation to be observed, even in our long-time simulations (see Fig. 5i). The transition from QCMP to BCC represents an intriguing phenomenon for future study, particularly in the context of crystal growth kinetics in a QCMP-BCC coexistence configuration.

In some instances, QCMP can emerge as the final ordered phase without the presence of BCC. Figure 5k, l illustrates such a case, where two σ-QCMP nuclei form and grow, being wetted by the local icosahedral order. In the liquid state, some PreBCC is observed. The physical mechanism of independent QCMP quasi-crystallisation is similar to that observed when BCC dominates, as seen in Fig. 5a. More detailed analyses are provided in Supplementary Fig. 8. When the two nuclei meet, growth slows down but continues. Although the interface between them exhibits different orientations, it is not as sharp as the interface in Fig. 5i. Their growth is also mediated by an intermediate liquid phase, which further confirms the much lower interfacial energy of liquid−σ-QCMP compared to liquid-BCC and liquid−A15-QCMP in Ta. Interestingly, we observe that in this case, the lifetime of local icosahedral order can be much longer than when BCC is the final phase (see Supplementary Fig. 9a, b). This is reasonable, as a QCMP nucleus consistently supports the presence of local icosahedral order at its surface.

Based on these observations, we propose that the liquid-phase-mediated two-step crystallisation mechanism may be universal in solid-solid phase transformations, though this requires further investigation. A recent study by Liang et al.[61] supports this idea, identifying the emergence of local disorder at the interface as a critical factor for the A15-BCC phase transformation in tungsten.

In the cases discussed above, we observe that the disorder-to-order phase transformation in Ta is notably complex, despite it being a single-component system. The emergence of medium-range orderings, formed by local icosahedral structures, leads to multiple crystallisation pathways. All these transformations deviate from the direct nucleation scenario predicted by CNT and proceed via non-classical pathways.

In contrast, the crystallisation process in Zr appears to be much more straightforward, as shown in Fig. 6, akin to observations in

colloidal suspensions[35,62,63]. The concentration of local icosahedral order in Zr is relatively low, and local icosahedral order form only short-range orderings (see Fig. 4 and the inset of Fig. 6), with notably short lifetimes (Supplementary Fig. 9c). This highlights the dependency of the properties of local icosahedral order on the ordering pathways in metallic liquids, which has been previously unrecognised.

During nucleation, the BCC nucleus primarily encounters frustration from local motifs with different crystal-like symmetries; however, their abundance is limited, resulting in relatively weak frustration and minimal impact on BCC nucleation[14]. Conversely, the abundance of PreBCC, as shown in Fig. 6, indicates a thick interface of BCC nuclei, facilitating rapid nucleation and growth[10]. This provides further insight into previous simulation observations regarding the reinforcement of BCC-like orderings during supercooling[14,24]. Once nucleated, BCC can expand swiftly by absorbing FCC and HCP orders.

Interestingly, a recent study employing a new model Zr[28] revealed the potential for $R_c < 10^{12}$ K/s when competition arises between BCC and fivefold polytetrahedral structural orderings. While the underlying physical mechanism remains elusive, this observation emphasises the significance of the structural ordering competition in controlling GFA of elemental metals. Investigating whether the atomic-scale mechanism observed in Ta applies to this new Zr model will aid in generalising our concepts to other systems, though this remains a topic for future research.

Discussion

In this study, we conducted computer simulations to investigate the crystallisation kinetics of two monatomic metals, Ta and Zr, which differ enormously in their glass-forming abilities. The thermodynamic origin of their distinct behaviours lies in the interfacial energy, as previously observed in model systems[9,30,36].

Previous studies of binary alloys[9,10] highlighted the importance of local chemical and topological orderings in phase transformations. In contrast, our study of single-component systems revealed that the formation of medium-range orders, particularly connected icosahedra, influences the nucleation process. These local orders frustrate BCC nucleation and promote quasi-crystallisation in Ta. Both crystallisation and quasi-crystallisation follow non-classical pathways, but with distinct manifestations: In Ta, BCC nucleation involves wetted crystal-like bond-orientational orders, while in quasi-crystallisation, transient icosahedral order at the local cluster level dominates the nucleation process. These two processes compete during solidification, and whichever pathway prevails reduces the GFA.

In Zr, however, only crystallisation occurs, with no quasi-crystallisation observed, and a thicker preordering layer reduces frustration. These findings explain the contrasting GFA of Ta and Zr and support experimental observations[6]. Our results offer insights into the microscopic mechanisms that influence glass formation—an understanding that has been a long-standing goal in the field. Moreover, the universal wetting effect at the solid-liquid interface observed in our MD simulations is consistent with experimental evidence from elemental Al[64].

While previous studies have proposed various concepts regarding the competition between different crystalline structures and their relationships with GFA (see, e.g. refs. 65–68), most of these discussions are conceptual or qualitative. Our work provides a quantitative analysis of crystallisation kinetics and atomic-scale pathways, highlighting the crucial role of competing ordering effects. We find that competition among crystal-like orders alone is insufficient to drive glass formation (as seen in Zr), but the 'balanced' competition between crystallisation and quasi-crystallisation facilitates glass formation in Ta. An excessive abundance of local icosahedral order promotes quasi-crystallisation, thereby reducing the GFA[14,15], a factor often overlooked in prior research.

Our results align with the seminal experimental work of Kelton et al.[25], who found that local icosahedral structures in supercooled liquids stabilise against crystallisation. Our study provides a deeper understanding of how quasi-crystalline nuclei are wetted by surrounding icosahedral order, reducing the structural gradient at the interface. This sheds light on the relationship between icosahedral order and GFA, a connection difficult to explore experimentally.

The 'confusion principle'[69,70] has been central to understanding MG formation, especially in multicomponent alloys. However, our research differs by focusing on monatomic metals, where we aim to identify minimal conditions influencing GFA. This approach is essential for addressing the complexity of glass formation in multicomponent systems, which remains a major challenge. Our study emphasises the importance of frustration and competing ordering effects in determining whether a liquid undergoes crystallisation or vitrification, a perspective that complements the confusion principle. This idea aligns with the theoretical framework of the two-order-parameter model developed by Tanaka[20]. According to this model, although the global free energy minimum favours the crystal phase, the presence of certain transient local structural orders considerably affects phase transformations, depending on how these orders interact with the stable phase. The role of local structural orders can vary from case to case. In our work, we present a microscopic understanding of how local structural orders at different length scales play a role in crystallisation and glass formation. Our analysis also provides insights into the physical mechanisms behind quasi-crystal formation, which may extend to other complex phases as well. In fact, understanding the formation of MGs and quasi-crystals appears to be interconnected, offering valuable perspectives on the nature of MGs.

In addition, our computational study, which used widely employed empirical potentials for Zr and Ta[6,37], provides valuable insights into the fundamental physics of glass formation. Although these models do not perfectly replicate real materials, they offer a simplified understanding of the process. The experimental observation that Ta can form a glass while Zr cannot, at a cooling rate of 10^{14} K/s, aligns qualitatively with our simulations.

We have also observed that altering the alloy composition in systems such as NiCu, TiAl, and binary patchy particle models[14] influences the competition between crystallisation and quasi-crystallisation, resulting in enhanced GFA. However, competition solely among crystalline orders is insufficient to produce a good glass-former. This suggests the existence of a general underlying rule governing glass formation, even though the presence of local chemical order adds complexity to these systems. Previous experimental works provide crucial support for the physical mechanism of quasi-crystallisation identified in our study[25,32]. These works primarily focus on either crystallisation or quasi-crystallisation in the context of glass formation. Our study provides a unified discussion of both processes, using Ta and Zr as model systems, and offers perspectives on phase transformations in other systems with considerable local icosahedral order.

We believe real materials involve more complex physical mechanisms, where topological and chemical orderings, along with their interactions, play crucial roles in determining material properties. We hope that more accurate empirical models will be developed to bridge the gap between simulations and real materials, thereby advancing our understanding of these systems.

From our simulations, we find that the abundance of metastable phases associated with distinct local structural orders can induce non-classical crystallisation pathways, providing a physical mechanism for the vitrification of chemical elements. This structural mechanism may also explain the improved thermal stability observed in multi-component bulk MGs, followed by subsequent nanocrystallisation[31].

Interestingly, the hierarchically ordered σ-QCMP, characterised by noisy $g(r)$, exhibits lower interfacial energy than more ordered phases like BCC-Ta and A15-QCMP. This lower interfacial energy, stemming from abundant medium-range icosahedral order, facilitates rapid nucleation and growth, competing with equilibrium crystal phases. During σ-QCMP growth, cluster attachment or the addition of local icosahedral order becomes the key mechanism, providing insights into quasi-crystal formation[33,71]. Interface properties play a critical role in QCMP growth, offering potential for interfacial engineering. The observed wetting effects in crystallisation and quasi-crystallisation highlight their importance in phase transformations. These non-classical pathways present challenges for the direct application of CNT[10].

Research on local icosahedral order in MGs has a long history, with substantial effort focused on understanding their physical mechanisms[1,15,23,25,27]. Our study, alongside prior work[9,10], aims to address this long-standing question. local icosahedral order in supercooled liquids appears to inhibit equilibrium crystal formation, rather than induce slow dynamics. The different lifetimes of local icosahedral order in Zr and Ta (Supplementary Fig. 9) suggest a strong dependence on the ordered phases and interatomic interactions—often overlooked in previous research.

The question of which interatomic interactions are key for forming local icosahedral order is central to understanding amorphous structures and glasses. We propose that a rugged-shaped potential model, favouring multiple local minima, likely promotes complex structures like short- and medium-range icosahedral orderings. Our analysis of the EAM potentials for Zr and Ta, presented in Supplementary Fig. 1, reveals that the pair potential for Ta exhibits two energy minima separated by a positive peak. This feature persists even after incorporating the embedding energy term, although the overall energy scale is modified in both systems. Additionally, at a larger distance of approximately 5 Å, Ta shows a shallow minimum. In contrast, such features are absent in Zr, whose total energy profile more closely resembles that of a typical Lennard-Jones potential. This finding aligns with Engel et al.[72], who used oscillating pair potentials to stabilise icosahedral structures. Future studies should explore how the EAM potential form influences microstructure.

Concerning the shape of the EAM potential, our results indicate that it is not necessary for a potential energy function to be smooth in order to accurately describe metals. For comparison, the smooth Lennard-Jones potential is known to be too simplistic for metallic systems. We also examined several other empirical potentials for metals, including machine-learning-based interatomic potentials for Mo and Ni[73], and a modified EAM potential for Cr[74]. In addition, we noted a newly developed physics-informed neural network potential for Ta[75]. All of these potentials have been benchmarked against experimental measurements and DFT calculations by their respective developers. As shown in Supplementary Fig. 10, the diatom energy curves of these potentials as a function of pair distance exhibit similarly rugged features, consistent with the behaviour seen for Ta in the EAM potential. Since chemical elements themselves are inherently complex, as discussed in this work, these observations suggest that the shape of the potential plays an important role in governing both material properties and the accuracy of interatomic potentials. This may serve as a key consideration in developing more sophisticated and transferable interatomic potentials in the future.

Medium-range orderings of icosahedra effectively hinder crystal nucleation but may promote the formation of QCMPs, leading to internal competition between quasi-crystallisation and crystallisation. Interfacial energy, dependent on structural orders, ultimately determines the final ordered phase. Desgranges and Delhommelle[53] observed a nonmonotonic behaviour of nucleation barriers in glass-forming copper alloys with remarkable local icosahedral order, especially at large supercooling, but not in a similar binary alloy with a much lower number density of local icosahedral order. This behaviour was attributed to the formation of centre-connected local icosahedral

order, accompanied by the increasing amount of close-packed structures. Our findings provide additional support for the notion that the appearance of competing phases or structures may elevate the interfacial energy and consequently substantially increase the nucleation barrier. The similarities and differences in underlying physical mechanisms warrant further investigation.

Although our current study focuses on single-component systems, a similar mechanism may extend to systems favouring local icosahedral order as the locally favoured structure, such as those interacting with the Dzugutov potential[76] and oscillating pair potentials[72], CuZr[77,78], AlSm[79], and many other multicomponent systems.

The non-classical crystallisation pathway challenges the assumption that CNT applies in simple single-component systems. In real materials, various non-classical pathways may be necessary to reduce the crystallisation barrier, highlighting the need for further studies to refine classical theory.

So far, our discussion has focused on MGs, concluding that both transition metals and metalloid-like single-component systems can vitrify. However, this insight can extend to other fields, such as monatomic metals, where GFA is not fully understood. A notable example is antimony (Sb), a phase-change material identified by Salinga et al.[80], which can rapidly switch between amorphous and crystalline states, making it promising for information storage. Another example is the vitrification of active metals like lithium (Li) and sodium (Na) through electrochemical deposition, crucial for developing high-performance batteries[81]. These examples are of crucial technological importance, but the mechanisms governing crystallisation kinetics and GFA are still unclear. We believe our study offers valuable insights that could advance the understanding of phase transformations in these monatomic metals and open up exciting avenues for future research.

Methods
Molecular dynamics simulations
Large-scale MD simulations were conducted to systematically study the crystallisation kinetics of two elemental metals, Ta and Zr, using the open-source software LAMMPS[82]. Each simulation involved a cubic box containing $N = 16,000$ atoms, simulated under the *NPT* ensemble (constant number, constant pressure, constant temperature) with $P = 0$. Initially, the samples were melted and equilibrated at temperatures well above their respective T_m of the stable phase for Ta and Zr, respectively[10]. Subsequently, they were cooled to the target temperatures until crystallisation occurred. The simulations utilised a time step of 0.002 ps and implemented periodic boundary conditions in all three dimensions. A total of 30 independent simulations were performed at each temperature to ensure robust statistical analysis. The data post-processing is partly finished by using our open-source Python package 'PyMatterSim'[83].

Finite-size effects are always an important consideration in computer simulations, although their influence varies depending on the specific research question. In our study, we focused primarily on results from simulations with $N = 16,000$ atoms. However, we also performed simulations with larger system sizes ($N = 31,250$ and $N = 54,000$) and found that N does not qualitatively affect our findings. We now discuss the potential effects of N on nucleation processes, statistics, and kinetics. As N increases, there are more opportunities for spatial-temporal fluctuations, which could facilitate the formation of multiple nuclei. (i) This could impact the nucleation time τ_{xtal}, and a system-size scaling relation, $\tau_{xtal} \sim 1/N$, might be expected, as suggested by Ingebrigtsen et al.[16]. However, our primary focus was on the differences in crystallisation kinetics between Zr and Ta, rather than the absolute nucleation times at the size limit. (ii) When multiple nuclei form, the analysis becomes more complex, as observed in simulations shown in Fig. 5 and Supplementary Figs. 7 and 8. For example, comparing Fig. 5a, k, we found that the presence of multiple nuclei does not

alter the microscopic nucleation process compared to a single nucleus. Moreover, the emergence of multiple nuclei can improve nucleation statistics by reducing the number of independent simulations required. This is why we performed 30 independent simulations for better statistical accuracy. Nevertheless, studying crystallisation in systems with even larger cells using more powerful computational resources remains an exciting avenue for future research.

Structural characterisation
We use combinations of bond-orientational order parameters to define the local structures in supercooled liquids[84]. Firstly, for a configuration, a complex vector for atom i is computed as

$$q_{lm}(i) = \frac{1}{N_i} \sum_{j=1}^{N_i} Y_{lm}(\theta(\mathbf{r}_{ij}), \phi(\mathbf{r}_{ij})), \qquad (4)$$

where N_i is the number of the nearest neighbours of atom i, $-l \le m \le l$, and Y_{lm} is the spherical harmonics. The coarse-grained order parameter Q_l is defined as $Q_l(i) = \sqrt{\frac{4\pi}{2l+1} \sum_{m=-l}^{l} |Q_{lm}(i)|^2}$, in which $Q_{lm}(i)$ is the average of $q_{lm}(i)$ over the first coordination shell, including atom i itself.

In our structural analyses, the coexistence of multiple structural orderings makes it difficult to characterise them simultaneously. For instance, a perfect local icosahedral order involves 12 neighbours, a perfect BCC structure requires 14 neighbours, and the structures of the σ and A15 phases extend over much longer ranges. To address this challenge, we consider varying numbers of nearest neighbours (N_i) to accurately characterise these structures using bond-orientational order parameters. Specifically, we use the following criteria: For BCC, we consider the nearest 14 particles ($N_i = 14$). For QCMP, we focus on atoms within a cutoff distance of 7.7 Å. For icosahedra, we examine the nearest 12 particles ($N_i = 12$). The cutoff for QCMP is determined based on the method by Keys and Glotzer[33], where they effectively characterised similar quasi-crystalline approximants in simulations of a single-component model liquid with a pair potential. By testing different trial cutoffs, we analysed the microstructures of the σ and A15 phases (see Fig. 1) and found that a combination of s_6 and s_{12} from Eq. (2) is sufficient to characterise the ordered local structures at this distance.

We utilise the parameter w_6 defined as

$$w_6 = \sum_{m_1 + m_2 + m_3 = 0} \begin{pmatrix} 6 & 6 & 6 \\ m_1 & m_2 & m_3 \end{pmatrix} q_{6m_1} q_{6m_2} q_{6m_3}, \qquad (5)$$

to identify the icosahedral centre ($w_6 < -0.023$)[55]. The term in parentheses represents the Wigner 3-*j* symbol. Similarly, normalised coarse-grained versions $\hat{W}_l$ ($l \in \{4, 6\}$) from Q_{lm} are utilised to characterise crystal-like bond-orientational orderings[10].

In practice, for each atom in a given configuration, we first determine whether it belongs to the BCC or QCMP phase, as these are mutually exclusive. Our analysis yielded the following findings: (1) $s_6 > 10$ is effective for identifying BCC particles, but not for other structures. Therefore, we use $s_6 > 10$ exclusively to assign atoms to the BCC phase. (2) $s_{12} > 50$ can identify particles belonging to the σ phase, A15 phase, or BCC phase. To distinguish between these, we combine $s_{12} > 50$ with $s_6 \le 10$ to assign atoms to the QCMP (σ/A15 phase). Next, we assess whether a particle exhibits icosahedral ordering by calculating w_6. To characterise crystal-like preordering, we group non-crystalline particles with $Q_6 > 0.25$ as follows: a particle is classified as belonging to a BCC-like crystal (PreBCC) if $W_6 > 0$, as FCC-like if $W_6 < 0$ and $W_4 < 0$, and as HCP-like if $W_6 < 0$ and $W_4 > 0$. These criteria have been validated in previous studies of single-component systems[9,44].

Melting temperature and enthalpy of fusion

We compute the melting temperature of a solid phase using the liquid-solid coexistence method. For each solid phase, we construct a rectangular simulation cell. Initially, 1/3 of the cell, located in the middle part, is frozen, while the rest of the system is heated to a high temperature to reach an equilibrated state. We then bring the entire system to a trial temperature and relax the system for 1.0 ns under the NPT ensemble. This process is repeated at various temperatures, and we monitor the time dependence of the potential energy. When the interfaces remain stable or the system's potential energy shows minimal change, we identify the corresponding temperature as T_m of the solid phase. The number of atoms is set as 48,672, 48,510, and 48,000 for A15-QCMP, σ-QCMP, and BCC phases of Ta, respectively, and 48,000 for Zr. As shown in Supplementary Fig. 3, the measured T_m for BCC, σ-QCMP, and A15-QCMP phases of Ta are $3255 \pm 5\,K$, $2985 \pm 5\,K$, and $2950 \pm 5\,K$, respectively. For Zr, the T_m for the BCC phase is $2105 \pm 5\,K$ (Supplementary Fig. 4). The measured T_m values for the BCC phase of Ta and Zr are in close agreement with previous studies[6,38]. Notably, BCC has a much higher T_m compared to the other metastable phases.

Inspired by the different T_m of the metastable phases compared to the stable phase in Ta, we calculate the enthalpy of fusion ΔH_m for each phase. To achieve this, we first generate a perfectly ordered solid phase configuration and heat it to its T_m. The system is then relaxed at this temperature for 1.0 ns, and we calculate the enthalpy $H_{(solid)}$. Next, the model is heated to a much higher temperature to melt it and reach an equilibrated liquid state. The liquid is then cooled back to T_m, and the system is relaxed for another 1.0 ns. The time dependence of the enthalpy for the liquid phase, $H_{(liquid)}$, is then computed. We used 16,224, 16,170, and 16,000 atoms for A15-QCMP, σ-QCMP, and BCC phases of Ta, respectively, and 16,000 atoms for Zr. The time dependence of the enthalpy for both the liquid and solid phases is shown in Supplementary Figs. 3 and 4. From this, we can extract ΔH_m accordingly. The thermodynamic driving force for crystallisation is then estimated empirically by the equation: $\Delta \mu_{L \to S}(T) = \Delta H_m(1 - T/T_m)$[85,86]. Additional computational details are provided in our previous work[10].

Liquid-solid interfacial energy analysis

At the melting temperature T_m, the liquid and solid phases have the same Gibbs free energy, which is equivalent to the same Helmholtz free energy at $P = 0$. However, the presence of an interface between the liquid and solid phases at T_m increases the system's free energy. Therefore, we aim to estimate the liquid-solid interfacial energy, γ, at T_m. We use the free energy perturbation method to estimate the excess free energy. Specifically, we approximate the free energy difference, ΔF, between state A (pure liquid phase) and state B (liquid-solid coexistence) using the exponential averaging method:

$$\Delta F(T_m) = -k_B T_m \ln < \exp\left[-\frac{\langle U_A(\{\mathbf{r}_i\}, t_0) \rangle - U_B(\{\mathbf{r}_i\}, t_0)}{k_B T_m}\right] >, \quad (6)$$

where $\mathbf{r}_i$ denotes the set of particle positions at a given state and U represents the corresponding potential energy at time t_0. In practice, we perform long-time simulations for the liquid phase at T_m (with $t > 1000\tau_\alpha(T_m)$, where τ_α is the structural relaxation time, which is small at high temperatures) to ensure comprehensive sampling. Additionally, we construct liquid-solid coexistence configurations between the liquid phase and different solid phases, using a planar interface design. We set the number of atoms as 48,672, 48,510, and 48,000 for A15-QCMP, σ-QCMP, and BCC phases of Ta, respectively, and 48,000 atoms for Zr. The system is then equilibrated at T_m to extract the potential energy. The liquid-solid interfacial energy is estimated from: $\gamma(T_m) = N_i \Delta F(T_m)/A_i$, where A_i is the interfacial area and N_i is the number of atoms belonging to the interface. To measure A_i more accurately, we perform morphology analysis using the alpha-shape method

implemented in OVITO[87,88]. The morphologies of the liquid-solid interfaces, excluding all other particles, are visualised in Supplementary Fig. 5. For Ta, we consider the solid phases as BCC, σ-QCMP, and A15-QCMP. For Zr, we focus only on the BCC phase. The distance of each particle from the interfaces is calculated. Given the distinct structural characteristics of the different phases, we consider both particle-level and cluster-level information for estimating N_i for the BCC and QCMP phases.

Diffusion rates

To assess the mobility of particles during crystallisation, we measure the liquid diffusion rate D by first calculating the mean-squared displacements, $\langle \Delta r^2(t) \rangle$, which is given by $\langle \Delta r^2(t) \rangle = \langle \sum [\mathbf{r}(t) - \mathbf{r}(0)]^2 \rangle / N$. In this process, we generate a liquid configuration and relax it at the target temperature for a sufficient time to ensure the system reaches equilibrium. The ensemble is then switched from the NPT (constant number, pressure, and temperature) to the NVT (constant number, volume, and temperature) ensemble for production runs. The NVT ensemble is used for convenience in data processing. Once the system reaches equilibrium, we ensure that $\langle \Delta r^2(t) \rangle$ enters the diffusive regime. The diffusion coefficient D is then calculated as D via $D(T) = \lim_{t \to \infty} \langle \Delta r^2(t) \rangle / 6t$. We note that for Zr, the temperature range available to measure D is limited by its poor GFA.

Data availability

All data that support the findings of this study are available in the article and the Supplementary Information. Source data are provided with this paper and have been deposited in figshare at https://doi.org/10.6084/m9.figshare.29655359.v1.

Code availability

All codes used for simulation and analysis are available from the corresponding authors upon request. The source codes used for data analysis are available from PyMatterSim (https://doi.org/10.6084/m9.figshare.29176556.v1).

References

1. Reichert, H. et al. Observation of five-fold local symmetry in liquid lead. *Nature* **408**, 839–841 (2000).
2. Zhang, J. & Zhao, Y. Formation of zirconium metallic glass. *Nature* **430**, 332–335 (2004).
3. Wang, Y. et al. Amorphouslike diffraction pattern in solid metallic titanium. *Phys. Rev. Lett.* **95**, 155501 (2005).
4. Hattori, T. et al. Does bulk metallic glass of elemental Zr and Ti exist? *Phys. Rev. Lett.* **96**, 255504 (2006).
5. Bhat, M. H. et al. Vitrification of a monatomic metallic liquid. *Nature* **448**, 787–790 (2007).
6. Zhong, L., Wang, J., Sheng, H., Zhang, Z. & Mao, S. X. Formation of monatomic metallic glasses through ultrafast liquid quenching. *Nature* **512**, 177–180 (2014).
7. Yuan, Y. et al. Three-dimensional atomic packing in amorphous solids with liquid-like structure. *Nat. Mater.* **21**, 95–102 (2022).
8. Klement, W., Willens, R. H. & Duwez, P. Non-crystalline structure in solidified gold-silicon alloys. *Nature* **187**, 869–870 (1960).
9. Hu, Y.-C. & Tanaka, H. Physical origin of glass formation from multicomponent systems. *Sci. Adv.* **6**, eabd2928 (2020).
10. Hu, Y.-C. & Tanaka, H. Revealing the role of liquid preordering in crystallisation of supercooled liquids. *Nat. Commun.* **13**, 4519 (2022).
11. Hu, Y.-C. & Tian, J. Data-driven prediction of the glass-forming ability of modeled alloys by supervised machine learning. *J. Mater. Inform.* **3**, 1 (2023).
12. Hu, Y.-C., Schroers, J., Shattuck, M. D. & O'Hern, C. S. Tuning the glass-forming ability of metallic glasses through energetic frustration. *Phys. Rev. Mater.* **3**, 085602 (2019).

13. Hu, Y.-C., Jin, W., Schroers, J., Shattuck, M. D. & O'Hern, C. S. Glass-forming ability of binary Lennard-Jones systems. *Phys. Rev. Mater.* **6**, 075601 (2022).

14. Hu, Y.-C. et al. Glass formation in binary alloys with different atomic symmetries. *Phys. Rev. Mater.* **4**, 105602 (2020).

15. Tanaka, H. Roles of local icosahedral chemical ordering in glass and quasicrystal formation in metallic glass formers. *J. Phys. Condens. Matter* **15**, L491 (2003).

16. Ingebrigtsen, T. S., Dyre, J. C., Schrøder, T. B. & Royall, C. P. Crystallization instability in glass-forming mixtures. *Phys. Rev. X* **9**, 031016 (2019).

17. Tanaka, H. Simple view of waterlike anomalies of atomic liquids with directional bonding. *Phys. Rev. B* **66**, 064202 (2002).

18. Tong, X. et al. Breaking the vitrification limitation of monatomic metals. *Nat. Mater.* **23**, 1193–1199 (2024).

19. Yang, Y. et al. Determining the three-dimensional atomic structure of an amorphous solid. *Nature* **592**, 60–64 (2021).

20. Tanaka, H. Bond orientational order in liquids: towards a unified description of water-like anomalies, liquid-liquid transition, glass transition, and crystallization. *Eur. Phys. J. E* **35**, 1–84 (2012).

21. Royall, C. P. & Williams, S. R. The role of local structure in dynamical arrest. *Phys. Rep.* **560**, 1–75 (2015).

22. Tanaka, H. Structural origin of dynamic heterogeneity in supercooled liquids. *J. Phys. Chem. B* **129**, 789–813 (2025).

23. Frank, F. C. Supercooling of liquids. *Proc. R. Soc. A* **215**, 43–46 (1952).

24. Jakse, N. & Pasturel, A. Local order of liquid and supercooled zirconium by ab initio molecular dynamics. *Phys. Rev. Lett.* **91**, 195501 (2003).

25. Kelton, K. F. et al. First x-ray scattering studies on electrostatically levitated metallic liquids: demonstrated influence of local icosahedral order on the nucleation barrier. *Phys. Rev. Lett.* **90**, 195504 (2003).

26. Sheng, H. W., Luo, W. K., Alamgir, F. M., Bai, J. M. & Ma, E. Atomic packing and short-to-medium-range order in metallic glasses. *Nature* **439**, 419–425 (2006).

27. Cheng, Y. Q. & Ma, E. Atomic-level structure and structure-property relationship in metallic glasses. *Prog. Mater. Sci.* **56**, 379–473 (2011).

28. Becker, S., Devijver, E., Molinier, R. & Jakse, N. Glass-forming ability of elemental zirconium. *Phys. Rev. B* **102**, 104205 (2020).

29. Schenk, T., Holland-Moritz, D., Simonet, V., Bellissent, R. & Herlach, D. Icosahedral short-range order in deeply undercooled metallic melts. *Phys. Rev. Lett.* **89**, 075507 (2002).

30. Shen, Y. T., Kim, T. H., Gangopadhyay, A. K. & Kelton, K. F. Icosahedral order, frustration, and the glass transition: evidence from time-dependent nucleation and supercooled liquid structure studies. *Phys. Rev. Lett.* **102**, 057801 (2009).

31. Wang, Q., Liu, C. T., Yang, Y., Dong, Y. D. & Lu, J. Atomic-scale structural evolution and stability of supercooled liquid of a Zr-based bulk metallic glass. *Phys. Rev. Lett.* **106**, 215505 (2011).

32. Kurtuldu, G., Shamlaye, K. F. & Löffler, J. F. Metastable quasicrystal-induced nucleation in a bulk glass-forming liquid. *Proc. Natl. Acad. Sci. USA* **115**, 6123–6128 (2018).

33. Keys, A. S. & Glotzer, S. C. How do quasicrystals grow? *Phys. Rev. Lett.* **99**, 235503 (2007).

34. Kelton, K. F. & Greer, A. L. *Nucleation in Condensed Matter: Applications in Materials and Biology* (Pergamon, 2010).

35. Kawasaki, T. & Tanaka, H. Formation of a crystal nucleus from liquid. *Proc. Natl. Acad. Sci. USA* **107**, 14036–14041 (2010).

36. Russo, J., Romano, F. & Tanaka, H. Glass forming ability in systems with competing orderings. *Phys. Rev. X* **8**, 021040 (2018).

37. Mendelev, M. I. et al. Development of suitable interatomic potentials for simulation of liquid and amorphous Cu-Zr alloys. *Philos. Mag.* **89**, 967–987 (2009).

38. Gunawardana, K. G. S. H., Wilson, S. R., Mendelev, M. I. & Song, X. Theoretical calculation of the melting curve of Cu-Zr binary alloys. *Phys. Rev. E* **90**, 052403 (2014).

39. Arias, D. & Abriata, J. P. Cu-Zr (copper-zirconium). *J. Ph. Equilib.* **11**, 452–459 (1990).

40. Arakcheeva, A., Chapuis, G., Birkedal, H., Pattison, P. & Grinevitch, V. The commensurate composite σ-structure of β-tantalum. *Acta Crystallogr. B* **59**, 324–336 (2003).

41. Tillmann, K., Thust, A., Gerber, A., Weides, M. P. & Urban, K. Atomic structure of β-Tantalum nanocrystallites. *Microsc. Microanal.* **11**, 534–544 (2005).

42. Jain, A. et al. The Materials Project: a materials genome approach to accelerating materials innovation. *APL Mater.* **1**, 011002 (2013).

43. Rein ten Wolde, P., Ruiz-Montero, M. J. & Frenkel, D. Numerical calculation of the rate of crystal nucleation in a Lennard-Jones system at moderate undercooling. *J. Chem. Phys.* **104**, 9932–9947 (1996).

44. Russo, J. & Tanaka, H. The microscopic pathway to crystallization in supercooled liquids. *Sci. Rep.* **2**, 505 (2012).

45. Lee, S., Bluemle, M. J. & Bates, F. S. Discovery of a Frank-Kasper σ phase in sphere-forming block copolymer melts. *Science* **330**, 349–353 (2010).

46. Pedersen, U. R., Schrøder, T. B., Dyre, J. C. & Harrowell, P. Geometry of slow structural fluctuations in a supercooled binary alloy. *Phys. Rev. Lett.* **104**, 105701 (2010).

47. Cortella, L. et al. Evidences of transitory metastable phases in refractory metals solidified from highly undercooled liquids in a drop tube. *Phys. Rev. Lett.* **70**, 1469–1472 (1993).

48. Jakse, N., Le Bacq, O. & Pasturel, A. Prediction of the local structure of liquid and supercooled tantalum. *Phys. Rev. B* **70**, 174203 (2004).

49. Becker, S., Devijver, E., Molinier, R. & Jakse, N. Unsupervised topological learning approach of crystal nucleation. *Sci. Rep.* **12**, 3195 (2022).

50. Lee, S., Leighton, C. & Bates, F. S. Sphericity and symmetry breaking in the formation of Frank-Kasper phases from one component materials. *Proc. Natl. Acad. Sci. USA* **111**, 17723–17731 (2014).

51. Cavagna, A. Supercooled liquids for pedestrians. *Phys. Rep.* **476**, 51–124 (2009).

52. Wu, Z. W., Li, M. Z., Wang, W. H. & Liu, K. X. Correlation between structural relaxation and connectivity of icosahedral clusters in CuZr metallic glass-forming liquids. *Phys. Rev. B* **88**, 054202 (2013).

53. Desgranges, C. & Delhommelle, J. Unusual crystallization behavior close to the glass transition. *Phys. Rev. Lett.* **120**, 115701 (2018).

54. Hu, Y.-C. et al. Configuration correlation governs slow dynamics of supercooled metallic liquids. *Proc. Natl. Acad. Sci. USA* **115**, 6375–6380 (2018).

55. Leocmach, M. & Tanaka, H. Roles of icosahedral and crystal-like order in the hard spheres glass transition. *Nat. Commun.* **3**, 974 (2012).

56. Peng, Y. et al. Two-step nucleation mechanism in solid-solid phase transitions. *Nat. Mater.* **14**, 101–108 (2015).

57. Tanaka, H., Hayashi, T. & Nishi, T. Digital image analysis of droplet patterns in polymer systems: point pattern. *J. Appl. Phys.* **65**, 4480–4495 (1989).

58. Russo, J. & Tanaka, H. Crystal nucleation as the ordering of multiple order parameters. *J. Chem. Phys.* **145**, 211801 (2016).

59. Duncan, J. et al. Collective atomic displacements during complex phase boundary migration in solid-solid phase transformations. *Phys. Rev. Lett.* **116**, 035701 (2016).

60. Rogal, J., Schneider, E. & Tuckerman, M. E. Neural-network-based path collective variables for enhanced sampling of phase transformations. *Phys. Rev. Lett.* **123**, 245701 (2019).

61. Liang, Y., Leines, G. D., Drautz, R. & Rogal, J. Structural transformations driven by local disorder at interfaces. *Phys. Rev. Mater.* **8**, 033402 (2024).

62. Gasser, U., Weeks, E. R., Schofield, A., Pusey, P. N. & Weitz, D. A. Real-space imaging of nucleation and growth in colloidal crystallization. *Science* **292**, 258–262 (2001).

63. Tan, P., Xu, N. & Xu, L. Visualizing kinetic pathways of homogeneous nucleation in colloidal crystallization. *Nat. Phys.* **10**, 73–79 (2014).

64. Oh, S. H., Kauffmann, Y., Scheu, C., Kaplan, W. D. & Rühle, M. Ordered liquid aluminum at the interface with sapphire. *Science* **310**, 661–663 (2005).

65. Inoue, A., Zhang, T. & Masumoto, T. Glass-forming ability of alloys. *J. Non Cryst. Solids* **156**, 473–480 (1993).

66. Waseda, Y., Chen, H.-S., Jacob, K. T. & Shibata, H. On the glass forming ability of liquid alloys. *Sci. Technol. Adv. Mater.* **9**, 023003 (2008).

67. Löffler, J. F. Bulk metallic glasses. *Intermetallics* **11**, 529–540 (2003).

68. Greer, A. L. Metallic glasses-on the threshold. *Mater. Today* **12**, 14–22 (2009).

69. Greer, A. L. Confusion by design. *Nature* **366**, 303–304 (1993).

70. Greer, A. L. Metallic glasses. *Science* **267**, 1947–1953 (1995).

71. Steinhardt, P. J. How does your quasicrystal grow? *Nature* **452**, 43–44 (2008).

72. Engel, M., Damasceno, P. F., Phillips, C. L. & Glotzer, S. C. Computational self-assembly of a one-component icosahedral quasicrystal. *Nat. Mater.* **14**, 104–116 (2015).

73. Zuo, Y. et al. Performance and cost assessment of machine learning interatomic potentials. *J. Phys. Chem. A* **124**, 731–745 (2020).

74. Choi, W.-M., Kim, Y., Seol, D. & Lee, B.-J. Modified embedded-atom method interatomic potentials for the Co-Cr, Co-Fe, Co-Mn, Cr-Mn and Mn-Ni binary systems. *Comput. Mater. Sci.* **130**, 121–129 (2017).

75. Lin, Y.-S., Pun, G. P. P. & Mishin, Y. Development of a physically-informed neural network interatomic potential for tantalum. *Comput. Mater. Sci.* **205**, 111180 (2022).

76. Dzugutov, M. Glass formation in a simple monatomic liquid with icosahedral inherent local order. *Phys. Rev. A* **46**, R2984–R2987 (1992).

77. Puosi, F. & Pasturel, A. Nucleation kinetics in a supercooled metallic glass former. *Acta Mater.* **174**, 387–397 (2019).

78. Ryltsev, R. E., Klumov, B. A., Chtchelkatchev, N. M. & Shunyaev, K. Y. Nucleation instability in supercooled Cu-Zr-Al glass-forming liquids. *J. Chem. Phys.* **149**, 164502 (2018).

79. Sun, Y. et al. Effects of dopants on the glass forming ability in Al-based metallic alloy. *Phys. Rev. Mater.* **3**, 023404 (2019).

80. Salinga, M. et al. Monatomic phase change memory. *Nat. Mater.* **17**, 681–685 (2018).

81. Wang, X. et al. Glassy Li metal anode for high-performance rechargeable Li batteries. *Nat. Mater.* **19**, 1339–1345 (2020).

82. Plimpton, S. Fast parallel algorithms for short-range molecular dynamics. *J. Comput. Phys.* **117**, 1–19 (1995).

83. Hu, Y. C. & Tian, J. PyMatterSim: a Python data analysis library for computer simulations of materials science, physics, chemistry, and beyond. Preprint at *arXiv* https://doi.org/10.48550/arXiv.2411.17970 (2024).

84. Steinhardt, P. J., Nelson, D. R. & Ronchetti, M. Bond-orientational order in liquids and glasses. *Phys. Rev. B* **28**, 784 (1983).

85. Turnbull, D. Kinetics of solidification of supercooled liquid mercury droplets. *J. Chem. Phys.* **20**, 411–424 (1952).

86. Kelton, K. F. Crystal nucleation in liquids and glasses. in *Solid State Physics* Vol. 45 (eds Ehrenreich, H. & Turnbull, D.) 75–177 (Academic Press, 1991).

87. Stukowski, A. Visualization and analysis of atomistic simulation data with OVITO—the open visualization tool. *Model. Simul. Mater. Sci. Eng.* **18**, 015012 (2009).

88. Stukowski, A. Computational analysis methods in atomistic modeling of crystals. *JOM* **66**, 399–407 (2014).

Author contributions

Y.C.H. and L.H.L. initiated and supervised the project with H.T. Y.C.H. and J.T.Z. performed the simulations. W.W.Z., H.Y.B. and W.H.W. contributed to the results discussion. Y.C.H. and H.T. wrote the paper.

Competing interests

The authors declare no competing interests.

Additional information

Supplementary information The online version contains supplementary material available at https://doi.org/10.1038/s41467-025-63221-8.

Correspondence and requests for materials should be addressed to Yuan-Chao Hu, Le-Hua Liu or Hajime Tanaka.

Peer review information *Nature Communications* thanks Nicholas Bailey and the other, anonymous, reviewer(s) for their contribution to the peer review of this work. A peer review file is available.

Reprints and permissions information is available at http://www.nature.com/reprints

Publisher's note Springer Nature remains neutral with regard to jurisdictional claims in published maps and institutional affiliations.